

1                   The Bayesian Earthquake Analysis Tool

2                   H. Vasyura-Bathke<sup>1,2</sup>, J. Dettmer<sup>3</sup>, A. Steinberg<sup>5</sup>, S. Heimann<sup>4</sup>, M. Isken<sup>5</sup>,  
                    O. Zielke<sup>1</sup>, P.M. Mai<sup>1</sup>, H. Sudhaus<sup>5</sup>, S. Jónsson<sup>1</sup>

<sup>1</sup> King Abdullah University of Science and Technology, Thuwal 23955-6900, Saudi Arabia

<sup>2</sup> Now at: University of Potsdam, D-14476 Potsdam, Germany

<sup>3</sup> University of Calgary, Calgary, Canada

<sup>4</sup> GFZ German Research Center for Geosciences, D-14469 Potsdam, Germany

<sup>5</sup> Department of Geoscience, Christian-Albrecht-University, Kiel, Germany

3                   February 19, 2020

4   Full address of first author:

5   Hannes Vasyura-Bathke

6   University of Potsdam

7   Institute for Geosciences

8   Karl-Liebknecht-Str. 24-25

9   14476 Potsdam-Golm Germany

## Abstract

The Bayesian Earthquake Analysis Tool (BEAT) is an open-source python software to conduct source-parameter estimation studies for crustal deformation events, such as earthquakes and magma intrusions, by employing a Bayesian framework with a flexible problem definition. The software features functionality to calculate Green's functions for a homogeneous or a layered elastic half-space. Furthermore, algorithm(s) that explore the solution space may be selected from a suite of implemented samplers. If desired, BEAT's modular architecture allows for easy implementation of additional features, for example, alternative sampling algorithms. We demonstrate the functionality and performance of the package using five earthquake source estimation examples: a full moment-tensor estimation; a double-couple moment-tensor estimation; an estimation for a rectangular finite source; a static finite fault estimation with variable slip; and a full kinematic finite fault estimation with variable hypocenter location, rupture velocity and rupture duration. This software integrates many aspects of source studies and provides an extensive framework for joint use of geodetic and seismic data for non-linear source- and noise-covariance estimation within layered elastic half-spaces. Furthermore, the software also provides an open platform for further methodological development and for reproducible source studies in the geophysical community.

## 1 Introduction

Crustal deformation processes, such as earthquakes, volcanic intrusions or due to human activities, can have severe socio-economic impacts. For appropriate hazard assessment of these phenomena, better understanding of the physical processes causing such deformation is required. An important step towards this goal is to carefully examine the geophysical observables caused by e.g. an earthquake rupture, and then use these data to infer the spatial and temporal evolution of the earthquake. The static surface deformation caused by such events can be measured by geodetic techniques such as global navigation satellite systems (GNSS, e.g. GPS, Galileo and Glonass) and Interferometric Synthetic Aperture Radar (InSAR) [e.g. [Jónsson et al., 2002](#); [Sudhaus and Jónsson, 2009](#); [Bathke et al., 2013](#)]. Rapid ground-surface displacements caused by a seismic wavefield, on the other hand, can be measured with seismometers and in some cases GNSS. Both types of measurements can be employed to study the characteristics of the deformation source by investi-

gating the inverse problem that relates source parameters to the observed data [e.g. [Kikuchi and Kanamori, 1982](#); [Yagi and Fukahata, 2011](#)].

Depending on the process being studied, the source can be parameterized in various ways. For example, to explain displacements caused by a magma intrusion in the crust, an isotropic moment tensor (MT) can sometimes be a reasonable approximation to model the observations [e.g. [Bathke et al., 2011](#); [Biggs et al., 2014](#)]. For earthquakes, a full or deviatoric MT [[Jost and Herrmann, 1989](#); [Tape and Tape, 2012](#); [Sokos et al., 2012](#); [Stähler and Sigloch, 2014](#); [Tape and Tape, 2015](#)] in combination with a single source-time function may be sufficient to explain seismological observations when the event is not large or is recorded at larger distances. However, the point-source assumption of the MT is generally not valid for earthquake ruptures. Therefore, finite sources with a spatial extent approximating earthquake fault planes have been applied. These include simple rectangular sources [[Haskell, 1964](#); [Okada, 1985](#)] and more complex finite-fault sources with hundreds of source parameters [e.g. [Olsen and Apsel, 1982](#); [Hartzell and Heaton, 1983](#); [Ji et al., 2002](#)]. The variety of finite fault representations that have been used is large, even for the same earthquake, as illustrated in the SRCMOD database [[Mai and Thingbaijam, 2014](#)].

For meaningful interpretation of estimation results, parameter uncertainties should be quantified. These uncertainties are mostly caused by measurement errors and theory errors [[Tarantola and Valette, 1982](#)]. The measurement error is partly due to data being contaminated by random noise during measurement. This noise at seismic stations can be reduced, for example, by employing better instruments and recording in low-noise environments. The most important error components in InSAR data are of atmospheric origin and may be reduced, for example, through using additional independent data or through advanced processing strategies [[Bekaert et al., 2015](#)]. Theory errors arise from assumptions in the mathematical formulation relating the model parameters to the observed data. For example, layered models that simplify the velocity structure of the Earth are used in the computation of Green’s functions [e.g. [Yagi and Fukahata, 2011](#); [Minson et al., 2013](#); [Duputel et al., 2014](#)]. Also, the parametrization of the deformation source, like the discretization of the earthquake fault plane into a fixed number of patches, introduces theory errors [[Dettmer et al., 2014](#)].

Parametrizations involving the source location, geometry and source-time-function are nonlin-

early related to the surface displacements caused by the source. Consequently, inferring the source parameters and uncertainties from displacements requires non-linear evaluation methods, which have high computational costs [Dettmer et al., 2007]. Bayesian inference is increasingly being applied to solve nonlinear estimation problems as it has the advantage of quantifying uncertainties of parameters [Monelli and Mai, 2008; Razafindrakoto and Mai, 2014] and prior information can be consistently integrated in the problem definition [Xu et al., 2015; Dutta et al., 2018].

Only a few software packages are available for nonlinear Bayesian inference combining static and dynamic displacement data (Tab. 1). For example, MTFit (Moment Tensor Fit) samples the parameters of a full moment tensor while fixing the centroid location [Pugh and White, 2018]. The algorithm considers amplitude ratios and the polarity of seismic phases. Although it does not support seismic waveforms, the software is useful for seismic events of low moment magnitudes ( $M_w \sim 3$ ). BayesISOLA (Bayesian Isolated Asperities) supports seismic waveforms to sample the parameters of a full moment tensor in a mixed linear-nonlinear setting [Vackář et al., 2017]. The location and source time are sampled via grid search and the moment-tensor components are determined with a linear least-squares inversion. GBIS (Geodetic Bayesian Inversion Software) provides a Bayesian framework for sources with simple geometrical shapes (prolate spheroid, penny-shaped crack, etc.) [Bagnardi and Hooper, 2018] that have analytic closed form solutions, assuming a homogeneous elastic half-space Earth structure. Due to these source parameterizations GBIS is limited to static surface displacement data, but can be useful in volcano geodesy (Tab. 1). While the advantages of using Bayesian inference in deformation source estimations are undeniable, a software package that is sufficiently general for a wide range of applications has been lacking.

In this work, we present the Bayesian Earthquake Analysis Tool (BEAT), a general suite of programs for a wide range of linear and nonlinear deformation source studies (Tab. 1, 2). BEAT provides the first open-source implementation for finite-fault estimations with variable static and/or kinematic slip parameters (including hypocenter location) using Bayesian inference. Our approach can include static and/or dynamic deformation data and the user can specify which seismic phases to include in the estimation. In addition, BEAT uses Green’s function databases [Heimann, 2011; Heimann et al., 2019] to speed up the source parameter estimations, where the user can also customize the 1D subsurface Earth structure. Finally, the software supports several sampling

algorithms that can be chosen depending on the problem to solve and the available computer resources. In conclusion, BEAT presents a complete open-source software infrastructure that can be applied to a wide range of problems and can also be extended by the user to foster future development of new methods, and to support reproducible research [Mai et al., 2016a,b].

## 2 Bayesian inference

To estimate model parameters of a selected deformation source from geodetic/seismic data we apply Bayesian inference. The posterior probability density of the model parameters  $p(\mathbf{m}|\mathbf{d}_{obs})$  can be obtained following Bayes' theorem

$$p(\mathbf{m}|\mathbf{d}_{obs}) \propto p(\mathbf{m})p(\mathbf{d}_{obs}|\mathbf{m}), \quad (1)$$

where  $\mathbf{m}$  is a vector of the parameters to estimate, i.e., the source parameters and optional hierarchical parameters (often called hyper-parameters), and  $\mathbf{d}_{obs}$  are observed data, i.e., seismic waveforms and/or geodetic surface displacements.

A priori information is expressed through  $p(\mathbf{m})$  for  $\mathbf{m}$ , and  $p(\mathbf{d}_{obs}|\mathbf{m})$  is the probability distribution of residuals (consisting of measurement and theory errors) for a given set of  $\mathbf{m}$ . For a given set of observed data,  $p(\mathbf{d}_{obs}|\mathbf{m})$  is interpreted as the likelihood function  $L(\mathbf{m})$ , which quantifies the probability that a particular set of model parameters gave rise to the data. The observed data  $\mathbf{d}_{obs}$  can be regarded as the real quantity  $\mathbf{d}_{real}$  in addition to measurement errors  $\mathbf{e}_{meas}$ ,

$$\mathbf{d}_{obs} = \mathbf{d}_{real} + \mathbf{e}_{meas}. \quad (2)$$

The forward model  $\mathbf{d}(\mathbf{m})$  simulates displacements generated by the chosen deformation source  $\mathbf{d}_{source}$  and includes theory errors  $\mathbf{e}_{th}$  [Tarantola and Valette, 1982],

$$\mathbf{d}(\mathbf{m}) = \mathbf{d}_{source} + \mathbf{e}_{th}. \quad (3)$$

The theory errors result from assumptions and simplifications in the mathematical formulation of the forward model, e.g., from assuming a simple subsurface model that differs from the true subsurface structure. Typically, measurement errors and theory errors are not exactly known independently and probability distributions are thus commonly assumed to represent these errors.

119 In this study, we are mostly investigating nonlinear problems for which no analytic solution ex-  
 120 ists. Therefore, we have to solve the problems numerically. We assume a multivariate Gaussian  
 121 distribution with error scaling  $\sigma_k$  to estimate the scale of the unknown distribution of residuals as  
 122 a hierarchical parameter for each dataset  $\mathbf{d}_{obs,k}$  [Fukuda and Johnson, 2008] of  $K$  datasets. Thus  
 123 the PPD becomes

$$p(\mathbf{m}, \sigma_1, \sigma_2, \dots, \sigma_K | \mathbf{d}_{obs,1}, \mathbf{d}_{obs,2}, \dots, \mathbf{d}_{obs,K}) \propto p(\mathbf{m}) \cdot \prod_{k=1}^K L(\mathbf{m}, \sigma_k), \quad (4)$$

124 with

$$L(\mathbf{m}, \sigma_k) = \frac{1}{(2\pi\sigma_k^2)^{N_k/2} |\mathbf{C}_{x_k}|^{1/2}} \exp \left[ -\frac{1}{2\sigma_k^2} (\mathbf{d}_{obs,k} - \mathbf{d}_k(\mathbf{m}))^T \mathbf{C}_{x_k}^{-1} (\mathbf{d}_{obs,k} - \mathbf{d}_k(\mathbf{m})) \right], \quad (5)$$

125 where  $\mathbf{d}(\mathbf{m})$  are the  $N_k$  predicted static or transient displacements for dataset  $k$ . The covariance  
 126 matrix  $\mathbf{C}_{x_k}$  describes the variances and covariances of residuals for each dataset. The inverses of the  
 127 covariance matrices in combination with the hierarchical scaling parameters  $\sigma_k$  act as weights for  
 128 the different datasets. While BEAT includes significant infrastructure for addressing the covariance  
 129 estimation, the details on the inference process are described elsewhere [Dettmer et al., 2007; Yagi  
 130 and Fukahata, 2011; Duputel et al., 2014; Hallo and Galovic, 2016].

## 131 2.1 Earth structure and Green’s Functions

132 Before computing data predictions  $\mathbf{d}(\mathbf{m})$  for a set of source mode parameters  $\mathbf{m}$ , we need to  
 133 make assumptions about the elastic subsurface structure. We assume the structure is a layered  
 134 elastic half-space described by the density, thickness, seismic wave velocity and attenuation of each  
 135 layer. Once the subsurface structure has been defined, a linear combination of 10 (8 for the far  
 136 field) elementary Green’s Functions (GFs) is needed to compute time-series of displacements for a  
 137 general moment-tensor source [Heimann, 2011; Heimann et al., 2019].

138 The GFs are numerically expensive to compute and it is thus advantageous to pre-compute a  
 139 database of GFs prior to the model parameter estimation. Here, the software library pyrocko-gf  
 140 is employed to generate databases of GFs [Heimann et al., 2019, 2017], which is an approach that  
 141 allows customizing the subsurface layering below each recording location. For example, the shallow  
 142 subsurface structure from the CRUST2.0 model [Bassin et al., 2000] could be included for each  
 143 station to complement a common global Earth structure below the crust [Kennett et al., 1995].

144 Estimation of the MT centroid location is possible once the GFs have been pre-computed for an  
145 appropriate source-receiver volume, which requires that the source region is discretized with a GF  
146 grid.

147 The GF databases are setup such that different programs can use them. Currently, support is  
148 included for QSEIS [Wang, 1999], QSSP [Wang et al., 2017] and PSGRN/PSCMP [Wang et al.,  
149 2006]. QSEIS calculates seismograms based on a layered visco-elastic half-space model and should  
150 be used if local or regional setups are of interest. QSSP calculates seismograms based on a layered,  
151 self-gravitating Earth and should be used for teleseismic setups or if interaction of the crust and  
152 atmosphere is important. PSGRN/PSCMP calculates synthetic stress, strain, displacement, tilt  
153 and gravitational fields on a layered visco-elastic halfspace and should be used for static displace-  
154 ment data.

155 Therefore, this infrastructure allows computing geodetic static displacements (at any depth) and  
156 seismic waveforms at any distance and depth range with desired frequency content. In addition,  
157 the open-source approach of BEAT makes extensions through user contributions straightforward  
158 to include.

## 159 **2.2 Estimation of source location and geometry**

160 The first order parameters of a deformation source are source location (east, north, depth), source-  
161 time-function (time, duration), and source geometry. These are determined in a nonlinear estima-  
162 tion (Eq. 5) and the number of source parameters  $\mathbf{m}$  depends on the choice of deformation source.  
163 BEAT supports a variety of point sources: a full moment tensor, an isotropic moment tensor,  
164 a double-couple moment tensor and a compensated linear vector dipole (CLVD) moment tensor  
165 (Tab. 2). By superposition of moment tensors, the GF database infrastructure permits discretizing  
166 finite sources of arbitrary geometry and temporal evolution. For example, the parameters of a  
167 rectangular source [Haskell, 1964; Heimann, 2011] with unknown rupture nucleation and rupture  
168 velocity can be inferred (Tab. 2, Supplemental Fig. S1, available in the electronic supplement to  
169 this article). BEAT also allows for multiple sources of the same type, each with a full and indepen-  
170 dent set of source model parameters, allowing for custom and complex model setups. With this  
171 flexible setup, complex source shapes, such as caldera ring faults [e.g. Bathke et al., 2015], faults

with variable strike and dip [e.g. Dutta et al., 2019] and curved dike intrusions [e.g. Chadwick et al., 2011] can be studied.

### 2.3 Estimation of the slip history on a finite fault

For a finite fault source, under the assumption that the source fault geometry is known, the aim is to resolve the spatio-temporal slip pattern on sub-faults. These sources are commonly discretized more finely than can be resolved by data (over-parameterization), which requires regularization to avoid unstable solutions due to the ill-posed inverse problem [Altman and Gondzio, 1999]. Regularization is typically applied via smoothness constraints based on a trade-off between slip smoothness and data fit [Jónsson et al., 2002]. In Bayesian inference, smoothing regularization can be achieved via a Gaussian prior  $p(\mathbf{s}|\alpha)$ , which includes a covariance matrix with off-diagonal terms, whose Cholesky decomposition is equivalent to a Laplacian finite difference operator  $\mathbf{L}$  of size  $M \times M$ . The trade-off parameter  $\alpha$  scales the degree of smoothing and can be assumed to be an unknown parameter (i.e., a hierarchical scaling that is estimated based on data information). Including smoothing regularization of slip values  $\mathbf{s}$  on  $M$  discretized fault patches, the PPD becomes [Fukuda and Johnson, 2008]

$$p(\mathbf{m}, \sigma_1, \sigma_2, \dots, \sigma_K | \mathbf{d}_{obs,1}, \mathbf{d}_{obs,2}, \dots, \mathbf{d}_{obs,K}) \propto p(\mathbf{m}) \cdot p(\mathbf{s}|\alpha) \cdot \prod_{k=1}^K p(\mathbf{d}_{obs,k} | \mathbf{m}, \sigma_k), \quad (6)$$

with

$$p(\mathbf{s}|\alpha) = \frac{|\mathbf{L}^T \mathbf{L}|^{1/2}}{(2\pi\alpha^2)^{M/2}} \exp \left[ -\frac{1}{2\alpha^2} (\mathbf{L}\mathbf{s})^T (\mathbf{L}\mathbf{s}) \right]. \quad (7)$$

Note that the application of Bayesian methods by themselves does not remove the need for regularization; it stems from the choice of spatial discretization of the fault. As long as the model is over-parametrized, regularization is needed. However, Bayesian model selection can be applied to overcome the need for regularization and subjective discretization choices [Dettmer et al., 2014].

For static geodetic data, the slip values on the fault patches are linearly related to the resulting surface displacements and  $\mathbf{d}(\mathbf{m})$  reduces to  $\mathbf{G}\mathbf{m}$ . Here,  $\mathbf{G}$  is the sensitivity kernel containing displacement GFs for a source with unit slip for each slip direction (slip-parallel and slip-perpendicular) on each sub-fault [Aki and Richards, 2002]. With seismic waveform data, kinematic rupture parameters can be estimated. These include hypocenter location and time, rupture velocity and the rupture duration. If rupture velocities are treated as an unknown velocity field on the fault, the

198 Eikonal equation can be solved in each forward operation to ensure causal rupture propagation  
199 [Minson et al., 2013]. This leads to nonlinearity and  $\mathbf{G}$  consists of two additional fields, i.e., the  
200 rupture duration and rupture start time on each slip patch for each seismic station.

201 In BEAT,  $\mathbf{G}$  is referred to as a `library` and can be assembled given the source geometry and  
202 the desired sub-fault discretization. This process requires a GF database to be pre-computed (see  
203 Sec. 2.1). When working with these `libraries`, it is useful to pre-compute them to make the  
204 numerical sampling of the posterior computationally tractable and more efficient. However, the  
205 `libraries` can be large for kinematic cases, leading to memory limitations. To overcome these  
206 limitations, we recommend to apply as much a priori information about the source parameters as  
207 possible when defining the problem. For example, the rupture velocity of an earthquake is likely to  
208 be close to the shear wave velocity of the subsurface medium [e.g. Das, 2015]. Consequently, the  
209 prior on the rupture velocity on each patch can be adjusted accordingly, if rupture propagation  
210 with super shear wave velocity is not expected.

### 211 3 Sampling algorithms

212 The posterior probability density (PPD) is usually numerically estimated through sampling with  
213 Markov Chain Monte Carlo (MCMC) methods [Sambridge and Mosegaard, 2002] or sequential  
214 Monte Carlo (SMC) methods [Moral et al., 2006]. A commonly-used algorithm in the family of  
215 MCMC samplers is Metropolis-Hastings sampling (MHS) [Metropolis et al., 1953]. In MHS, the  
216 solution space is explored by a random walk, where the direction and size (or length) of a step is  
217 randomly proposed by drawing from a probability distribution [Hastings, 1970]. A new state in  
218 the random walk is accepted or rejected probabilistically; if the new state has a higher or equal  
219 posterior probability than the current state, the new state is always accepted. If the new state has  
220 a lower posterior probability, the new state is sometimes accepted and sometimes rejected. This  
221 algorithm, samples directly from the PPD and allows to estimate general distributions where no  
222 closed-form solutions are available.

223 However, nonlinear source estimations often result in complex, multi-modal solutions that re-  
224 quire advanced sampling algorithms in order to fully sample the complex multidimensional PPD  
225 and to avoid misleading results. For BEAT, we implemented three advanced sampling algorithms:

Adaptive Metropolis-Hastings (AMH) [Roberts and Rosenthal, 2001], Sequential Monte Carlo (SMC) [Jarzynski, 1997; Neal, 2001; Moral et al., 2006; Ching and Chen, 2007; Minson et al., 2013] and Parallel Tempering (PT) [Geyer, 1991; Jasra et al., 2007; Dettmer and Dosso, 2012]. In the following paragraphs, we give a short description of each algorithm and refer the reader to the original publications for details.

The Adaptive Metropolis-Hastings algorithm tunes the step size of the proposal distribution based on the acceptance rate of the last  $N$  samples. If the acceptance rate is low, smaller steps are proposed and vice versa. This algorithm is useful when sampling problems with only a few model parameters; for example when estimating an isotropic moment tensor from geodetic data to resolve the location and volume change of a point source underneath a volcano [Kumagai et al., 2014].

In higher-dimensional problems, particularly with seismic data, the AMH algorithm appears to be insufficient. Here, the SMC algorithm performs better due to its ability to temper the likelihood, apply resampling, and to take advantage of parallel computing. In the SMC algorithm, samples are obtained by simulating a sequence of intermediate distributions from the prior to the posterior. Each sample starts from the prior and follows a trajectory through the intermediate distributions to the posterior, where it is independent from other samples. The transitioning between distributions is typically achieved by scaling from the prior to the posterior via an annealing parameter that allows samples to initially move freely in the parameter space, but gradually becomes more constrained by the data as the sample approaches the posterior. At various stages, resampling can be applied to refocus the large number of samples into regions of high likelihood. This process also helps the algorithm to avoid local minima. While slowly decreasing the annealing parameter for each trajectory, a sample transitions through the bridging distributions until the PPD is sampled. The annealing enables sampling of complex, multi-modal and highly peaked distributions since data information is gradually introduced. However, the number of trajectories needs to be sufficiently large with respect to the number of parameters [Minson et al., 2013]. We implemented the SMC algorithm with python’s multiprocessing library, and consequently, this implementation cannot scale beyond a single node of a computer cluster.

For parallel computing architectures (e.g. computer clusters), we implemented the PT algo-

255 rithm with the Message Passing Interface (MPI). This algorithm generates many MCMC chains  
 256 in parallel (one per CPU), which draw samples from a joint posterior that includes the target  
 257 posterior as well as tempered posteriors where the likelihood function is raised to a power of less  
 258 than unity. The chains are typically split such that half of the chains sample the target posterior  
 259 while the other half sample the tempered distributions. In addition, PT includes exchange moves,  
 260 where various chains communicate and exchange information by swapping parameter vectors  $\mathbf{m}$ .  
 261 The tempered posteriors significantly help the algorithm to widely explore the parameter space  
 262 and reduce the tendency of getting stuck in modes.

## 263 4 Seismic covariance-matrix structure

264 In BEAT, the covariance matrices  $\mathbf{C}_x$  for the seismic waveforms are estimated during the sampling,  
 265 based on data information and assumptions on the noise structure. It is important to note that  
 266 the noise covariance matrix substantially influences the Bayesian estimation result [Dettmer et al.,  
 267 2007; Duputel et al., 2012]. This matrix is generally not known a priori and it therefore has to be  
 268 considered as a part of the estimation problem. However, as the residuals include theory errors  
 269 (see Eqs. 2, 3), this task is not trivial. In BEAT, three different forms of the covariance matrix  
 270 are currently available: `variance`, `exponential(toeplitz)`, `non-toeplitz`. For the `variance` and  
 271 `exponential` forms, the data variance is estimated from the seismic data by analyzing the data  
 272 variability prior to the P-phase arrival. The `non-toeplitz` matrix on the other hand, is estimated  
 273 with an iterative approach and is based on the residual waveforms for the maximum a-posterior  
 274 (MAP) model parameters [Dettmer et al., 2007]. The non-Toeplitz covariance matrix accounts for  
 275 both non-stationary and correlated noise. As it is based on the residuals, it includes the effects  
 276 of both measurement errors and theory errors, e.g. due to inaccurate velocity structure of the  
 277 subsurface.

## 278 5 Software features

279 BEAT is written in the python programming language and provides a Bayesian sampling frame-  
 280 work for deformation source estimation. The project website, program prerequisites, platform and

license information can be found in Section 8. Several parts of BEAT are based on the `pyrocko` seismological toolbox [Heimann et al., 2017]. The programming structure is object-oriented and designed around two main estimation problems, which are referred to as `modes` and illustrated in Fig. 1. The first mode, `geometry`, addresses the nonlinear problem of estimating the geometry, source-time-function, location and magnitude or slip of the deformation sources (Sec. 2.2). The second mode, `ffi` (finite fault inversion), is used to estimate the spatially-variable static-slip values or kinematic rupture parameters (Sec. 2.3). While the modes can operate independently, we recommend to apply a `geometry` estimation prior to an `ffi` estimation. For example, if a `geometry` estimation for a magnitude  $M_w > 6.5$  earthquake yields a fault plane striking between 130 and 140 degrees, this information can be used in the `ffi` mode to constrain the fault geometry. Otherwise, a reference fault geometry must be specified from other information.

A problem-specific `yaml`-configuration file (e.g. `config_geometry.yaml` in Fig. 2) provides an interface for the user to adjust the various parameters of the problem, including prior information, data processing, and sampling-algorithm tuning. Two `datatypes` are supported in BEAT: `seismic` (waveforms) and `geodetic` (GNSS and InSAR static displacements). The data types are implemented in terms of `composites` that can be combined in the problem setup (Fig. 1). The `problem` and `composites` classes include the formulation of the posterior likelihood (eq. 5), which is then synthesized to the `model` (Fig. 1) object that can be used by any sampler to explore the solution space of the PPD. For numerical efficiency, the `model` is implemented via the open-source libraries `theano` and `pymc3`, which provide the option to translate python code to C code, making it computationally more efficient, or to CUDA C code to make use of graphical processing units (GPUs).

When using the software, the directory structure of the working directory gradually grows (Fig. 2). For example, the `mode` specific directories, such as `geometry`, are created during the course of the sampling and the `figures` directory after the results are plotted.

## 6 Application Examples

To demonstrate the capabilities of BEAT, we present five different source estimation examples. For the first example, we generated seismic waveforms from a MT point source and contami-

309 nated them with synthetic correlated noise. These synthetic data were then used to estimate the  
 310 components of a full MT. In the other four examples, we considered both geodetic and seismic  
 311 data of the 2009 L'Aquila earthquake. First, we estimate the location and the parameters of a  
 312 double-couple point source. Then, we employed a rectangular source to estimate the fault ge-  
 313 ometry of the rupture assuming uniform slip. With the MAP parameters from the rectangular  
 314 fault solution we then estimate spatially variable static slip, while keeping the fault geometry  
 315 fixed. Finally, we estimated kinematic parameters of the rupture based on the results of the pre-  
 316 vious two steps. Here, hypocentral location, rupture velocity and rupture duration were treated  
 317 as unknowns. These scenarios are fully reproducible and available as step-by-step tutorials at  
 318 <https://hvasbath.github.io/beat/examples/index.html>.

319 The uncertainty-quantification capability of BEAT and its flexibility can result in significant  
 320 computational costs. The overall computation time depends on the amount of data, the complexity  
 321 of the source parametrization, and the available computational resources. In the following, we will  
 322 provide approximate computation times for the five estimation examples.

## 323 **6.1 Example 1: Full Moment Tensor**

324 Here, we used the **geometry** mode to estimate parameters of a Mw5.5 MT source from simulated  
 325 seismic data at regional distances up to 1000 km (Supplemental Fig. S2, available in the electronic  
 326 supplement to this article). Simulated waveforms were computed using a double-couple MT source  
 327 with a sinusoidal source-time-function (on  $[0, \pi]$ ) and the simulated waveforms (Figs. S3 & S4 avail-  
 328 able in the electronic supplement to this article) were contaminated with simulated, temporally  
 329 and spatially correlated noise. To obtain such correlated noise for each waveform, we summed  
 330 up 300 synthesized waveforms containing the signals of random, full moment tensor sources in the  
 331 epicentral region ( $\pm 3$  km) with magnitudes between 3.0 and 4.7 and including five larger magnitude  
 332 sources between 4.5 and 5.0 with random source time variations between -20 and 5 seconds with  
 333 respect to the reference event. The corresponding signal-to-noise ratio varies between 1.2 and 3.3.  
 334 We applied SMC sampling with a **MTsource** parametrization to sample the parameters of a full  
 335 moment tensor, its centroid location and its source-time function.

336 To demonstrate the influence of different parametrizations for the data error covariance matrix

(Sec. 4), we compared results of sampling based on a diagonal covariance matrix (uncorrelated noise, `variance` type in BEAT) and a non-Toeplitz, full covariance matrix, which accounts for time-dependent and non-stationary noise [Dettmer et al., 2007]. The comparison shows that the double-couple mechanism was not retrieved in the estimation when neglecting noise correlations (Fig. 3a,c), but was well recovered when using a `non-toeplitz` covariance matrix (Fig. 3b,d). With only data noise contamination in this synthetic test, the uncertainty of the solution is low for the `variance` covariance-matrix case and the data are overfitted (Supplemental Fig. S5, S6 available in the electronic supplement to this article). However, this overfitting was reduced by using non-Toeplitz covariance matrices and the resulting parameter marginals are less biased (Supplemental Fig. S7, S8, S9 available in the electronic supplement to this article), than when diagonal covariance matrices were used.

For this example, we used 4 CPU cores on a standard mobile computer. We configured the SMC sampler with 2,000 Markov chains over 300 steps over 40 stages. During the sampling, the forward model was evaluated 24 million times, which took about 4 hours.

## 6.2 Example 2: Double-Couple Moment Tensor

We considered data from the 2009 L'Aquila earthquake to estimate the double-couple moment-tensor (DCSource) using the `geometry` mode of BEAT. We included P waveforms from 35 seismic stations at teleseismic distances between 30 to 90 degrees (Supplemental Fig. S10, available in the electronic supplement to this article). The seismic data were filtered with a Butterworth bandpass filter between 0.01 and 0.2 Hz. We applied a time window of -10 to +40 seconds around the theoretical P-phase arrival time to calculate the posterior probability at each station. For the seismic data we utilized the AK135 Earth velocity structure [Kennett et al., 1995] to compute a GF database with QSSP [Wang et al., 2017]. To compare the results for two sampling algorithms on the PPD, we used PT and SMC sampling with the same setup.

For both sampling algorithms (PT and SMC), the mode and MAP of the marginals are similar (Fig. 4). The estimated uncertainties in the source parameters are larger for PT compared to SMC. Fuzzy waveform misfits (Supplemental Figs. S11, S12 available in the electronic supplement to this article) are comparable and uncertainties obtained from the SMC algorithm might be un-

derestimated. These differences highlight that there is neither an ultimate measure nor a guarantee for convergence of sampling algorithms and the user must carefully evaluate posterior marginals estimated by the samplers [Mosegaard, 2012].

We configured the PT sampler with 20 chains and we randomly applied swaps every 10 to 30 steps. After each swap, we stored the sample of each Markov Chain that was sampled from the target PPD until 400k samples had been collected, which resulted in  $\sim 60$  million forward evaluations and required  $\sim 5$  hours of runtime. The SMC sampler was run with 5,000 Markov Chains and 400 steps that resulted in 31 stages where the forward model has been evaluated  $\sim 62$  million times and required  $\sim 6$  hours of runtime.

### 6.3 Example 3: Rectangular Source Fault estimation

Here, we used the seismic data from Example 2, and complement them with geodetic data to estimate the fault dimensions and geometry for the L'Aquila earthquake using the `geometry` mode of BEAT. The geodetic data were comprised of two InSAR surface displacement maps, derived from Envisat satellite images acquired before and after the earthquake from both ascending and descending acquisition geometries (Supplemental Tab. S1, available in the electronic supplement to this article). We applied the `kite` software [Isken et al., 2017] to spatially downsample the interferograms and to estimate the full data error variance-covariance matrix [Sudhaus and Jónsson, 2009; Jolivet et al., 2012]. The AK135 Earth velocity structure [Kennett et al., 1995] was applied to compute a GF database for the geodetic data with PSGRN/PSCMP [Wang et al., 2006]. The frequency band for the seismic data is broad compared to the previous example with 0.001 Hz to 0.1 Hz, because the rectangular source with the rupture propagating across the fault produces broad spectra.

We applied the SMC algorithm, a rectangular source parametrization and a non-Toeplitz seismic covariance matrix to estimate the location, orientation, extent and slip of the L'Aquila source fault (Supplemental Fig. S1, available in the electronic supplement to this article). In addition, we estimated the rupture nucleation point assuming a constant rupture velocity of 3.5 km/s as well as a source start time and duration of a half-sinusoidal source-time function. Finally, a hierarchical scaling was estimated (Eq. 4) for the interferograms and seismic data, as well as a bilinear ramp

function to account for possible inaccuracies in the satellite orbit information.

The results show that the strongest parameter trade-offs are between the extent of the fault (width and length), fault slip and the depth of the upper edge of the fault (Fig. 5). The horizontal location of the rupture nucleation point is well constrained and located near the western edge of the fault (nucleation\_x: -1 at left edge and 1 at right edge), while its downdip location is more uncertain, located somewhere near the bottom edge of the fault (nucleation\_y: -1 at the top edge and 1 at bottom edge). The MAP model can explain the static surface displacement data well (Supplemental Fig. S13, available in the electronic supplement to this article) and the simulated waveforms also show a good agreement with the observations, considering that only uniform fault slip was included in this model estimation (Supplemental Fig. S14, available in the electronic supplement to this article).

In this example, we again used 4 mobile CPU cores to sample 1,000 Markov chains with 100 steps each and through 22 stages of the SMC sampler. This resulted in  $\sim 2.2$  million forward evaluations and over 11 hours of computation time.

#### 6.4 Example 4: Static slip-distribution estimation with Laplacian smoothing

In this example we consider a finite fault parametrization for the L'Aquila earthquake and the `ffi` mode of BEAT using the static InSAR data. We employed the previously determined parameters from the rectangular source estimation (Sec. 6.3) to fix the source fault location and geometry as well as the orbital ramps for the InSAR scenes. We extended the previously obtained MAP fault dimensions in length by a factor of 1.6 and in width by a factor of 1.4. Then, we discretized the fault into  $2 \times 2$  km patches resulting in 121 patches ( $11 \times 11$ ). For each of these patches, we computed GFs slip-parallel and perpendicular to fault rake. While assuming smooth slip on neighboring patches (Laplacian smoothing; Eq. 7), we applied the SMC algorithm to solve for the two slip parameters on each patch as well as estimating the smoothing parameter and hierarchical scaling for each interferogram (Eq. 4). The number of parameters estimated in this example is 245, i.e., two slip parameters for each patch, one smoothing parameter and two hierarchical scaling parameters. To initialize each Markov Chain at a reasonable starting point of the high-dimensional search space,

we drew a random smoothing weight  $\alpha$  from its prior (uniform) distribution. With these smoothing values we inverted for the rake-parallel slip distribution via regularized non-negative least-squares [Fukuda and Johnson, 2008]. The resulting slip vectors in the slip-parallel direction and zero slip in the slip-perpendicular direction were set as the starting points for the MCs in the first stage of the SMC algorithm.

The fault slip distribution results (Fig. 6) show a maximum slip of  $\sim 0.7$  m and significant slip confined between 2 and 18 km. The slip uncertainties increase with depth as the ability of static surface displacements to resolve fault slip decreases with depth. This solution does not consider uncertainties in location and geometry as found in Example 3 (Fig. 5). These would enlarge the slip vector error ellipses [Sudhaus and Jónsson, 2009, 2011]. The model prediction of this variable fault slip model fits the observed InSAR data better than the previous constant slip model (Supplemental Fig. S15, available in the electronic supplement to this article).

We carried out this model parameter estimation on 4 mobile CPU cores as before and included sampling of 3,000 Markov chains for 300 steps over 43 stages of the SMC sampler. During the sampling the forward model was evaluated 39 million times, which took about 3 hours.

The assumption of smooth slip between neighboring slip patches can sometimes be inappropriate [Minson et al., 2013; Duputel et al., 2014; Ragon et al., 2018]. Thus, BEAT also supports estimating distributed slip without a Laplacian smoothing prior, but instead the uncertainty in Earth structure is propagated [Duputel et al., 2014] (Supplemental Sec. 1, Figs. S16-S22, available in the electronic supplement to this article).

## 6.5 Example 5: Kinematic nonlinear slip estimation with Laplacian smoothing

In this final example we extended the L'Aquila source estimation to include rupture kinematics and used both seismic waveforms and static InSAR data as observations. To increase the data information about the rupture details, we filtered the waveforms with an upper limit of 0.5 Hz and we extended time windows around P-wave arrivals to -10 s to 50 s. For the estimation, we applied the `ffi` mode of BEAT and used the posterior slip distribution result of example 4 as a slip prior to reduce the parameter space. The kinematic rupture parameters that we estimated include the

hypocenter time and location as well as the rupture velocity and duration on each fault patch. In addition, we estimated smoothing parameter  $\alpha$  and hierarchical residual scaling parameters. The total parameter count in this example is 491, i.e., four kinematic slip parameters for each of the 121 patches, three hypocenter parameters, one smoothing parameter, and three scaling parameters for the two InSAR datasets and the seismic data. We applied the SMC sampler in the estimation, assuming a non-Toeplitz seismic covariance matrix, with Markov Chains initialized to the posterior from the previous example, as we considered it as prior information.

The kinematic results show that the hypocenter location is well constrained, and that the rupture nucleated near the western edge of the fault at a depth between 10 and 12 km (Fig. 7 a). The rupture appears to have spread with near constant rupture velocity of  $\sim 3$  km/s across the fault. Compared to the static solution, the maximum slip is reduced to  $\sim 0.6$  m and the slip distribution is overall somewhat shallower (by  $\sim 2$  km), i.e., it is now mostly confined to depths less than 16 km. Due to the addition of seismic data, rake and slip uncertainties on deep slip patches are significantly reduced. Marginal distributions of selected patches (Supplemental Fig. S23, available in the electronic supplement to this article) show that the kinematic slip parameters for patches far from the hypocenter (e.g. patch 15) are poorly resolved, with the 95% confidence bounds on the rupture duration and rupture velocity, between 0.5 and 2.6 seconds and between 2.5 and 4.3 km/s, respectively. This is not be surprising as only teleseismic data were used in the estimation. Patches with high slip values have shorter rupture durations (e.g. patch 51) with the 95% confidence bounds between 0.1 and 2 seconds. The rupture velocities of patches close to the hypocenter (e.g. patch 67) are slightly better constrained (with the 95% confidence bounds between 2.45 and 3.8 km/s) than patches further away. Note that this kinematic solution includes an estimation of the smoothing weight  $\alpha$  and the result is based on a range of  $\alpha$  values rather than a single fixed smoothing value (Fig. 7 c). The moment rate function shows a source rupture duration of  $\sim 9$ -10 s with the peak moment release occurring between 4 s and 6 s (Fig. 7 b). The fit with the geodetic data is comparable to Example 4 (Fig. 8), but the fit with the seismic waveforms (Fig. 9) appears to be poorer than in Examples 2 and 3. The latter comparison, however, is unfair as the seismic data in this example include significantly more details due to the increased upper cut-off frequency of the bandpass filter.

Several features from our results generally agree with previous studies. The rupture exhibits predominantly a single slip region at depths between 5 and 16 km. The hypocenter is located in the northwest and offset from the main slip region [Cirella et al., 2009; Zhang et al., 2012]. The moment rate function (Fig. 7) shows a small peak near 2 s. Finally, the rake angle indicates a slight rotation of the slip vector with increasing depth [Zhang et al., 2012].

In this example we employed 25 cores on a workstation to sample 10,000 Markov chains for 300 steps over 35 stages of the SMC sampler. This resulted in  $\sim 100$  million forward model evaluations and a runtime of  $\sim 85$  hours.

## 7 Conclusions

The Bayesian Earthquake Analysis Tool (BEAT) is a new software for source estimations and uncertainty quantification in deformation source studies. It is open source and available under the license GPL3.0 and can be downloaded at <https://github.com/hvasbath/beat> [Vasyura-Bathke et al., 2019]. BEAT provides an extensive open source framework to study earthquake sources with various parameterizations, including moment-tensor point sources, rectangular static and kinematic sources, and static and kinematic finite fault sources. An important aspect of BEAT's contribution is the integration of multiple methods in a unified platform. In addition, we provide the novel ability to consider joint inversion of geodetic and seismic data for sources in a stratified, elastic half space with residual covariance estimation, while allowing fully non-linear treatment of all sources in a Bayesian framework. The intention behind providing such a unified framework to the geophysics community is to make research more reproducible and to accelerate the development of comprehensive tools for deformation source studies. The five examples presented here demonstrate the main functionalities of the BEAT software and can be reproduced through step-by-step tutorials available on the project website: <https://hvasbath.github.io/beat/examples/index.html>.

## 8 Data and Ressources

The BEAT package runs under Linux and MacOS on python versions  $\leq 3.5$  and is available at <https://github.com/hvasbath/beat> [Vasyura-Bathke et al., 2019]. It is distributed under the

GNU General Public Licence, version 3.0 and depends on the following main python libraries (and dependencies within): pyrocko [Heimann et al., 2017], pymc3 [Salvatier et al., 2015], Theano [Theano Development Team, 2016] and MPI4py [Dalcin et al., 2011].

The presented examples can be reproduced following the tutorials at: <https://hvasbath.github.io/beat/examples/index.html>.

Seismic waveforms were originally downloaded from Incorporated Research Institutions for Seismology (IRIS) <https://ds.iris.edu>. Envisat satellite radar data were provided by the European Space Agency (ESA) <https://earth.esa.int/web/guest/home>.

All of the figures have been produced by using matplotlib [Hunter, 2007] and can be generated through the BEAT plot command. Some maps have been produced by using Cartopy [Met Office, 2015].

Supplemental Material for this article includes a pdf file further illustrating the examples.

## 9 Acknowledgements

We thank Jiří Vackář, Romain Jolivet, one anonymous reviewer and the editor for their comments that helped to improve the quality of this manuscript. This research was supported by King Abdullah University of Science and Technology (KAUST), under award numbers BAS/1/1353-01-01 and BAS/1/1339-01-1. H.V-B was partially supported by Geo.X, the Research Network for Geosciences in Berlin and Potsdam under the project number SO\_087\_GeoX. H.S., A.S. and M.I. acknowledge founding by the German Research Foundation (DFG) through an Emmy-Noether Young Researcher Grant (276464525). I owe the most gratitude to my beloved wife Olha for her tireless support and tolerance during many evenings and nights spent writing the code and this manuscript.

## References

- Aki, K. and Richards, P. G. (2002). *Quantitative seismology*. University Science Books, 2 edition.
- Altman, A. and Gondzio, J. (1999). Regularized symmetric indefinite systems in interior point methods for linear and quadratic optimization. *Optimization Meth. & Soft.*, 11(1-4):275–302.
- Atzori, S. and Antonioli, A. (2011). Optimal fault resolution in geodetic inversion of coseismic data. *Geophys. J. Int.*, 185(1):529–538.
- Bagnardi, M. and Hooper, A. (2018). Inversion of surface deformation data for rapid estimates of source parameters and uncertainties: A Bayesian approach. *Geochemistry, Geophysics, Geosystems*, 19:1–18.
- Bassin, C., Laske, G., and Masters, G. (2000). The current limits of resolution for surface wave tomography in North America. *EOS Trans. AGU*, 81(F897).
- Bathke, H., Nikkhoo, M., Holohan, E., and Walter, T. (2015). Insights into the 3D architecture of an active caldera ring-fault at Tendürek volcano through modeling of geodetic data. *Earth Planet. Sci. Lett.*, 422:157–168.
- Bathke, H., Shirzaei, M., and Walter, T. R. (2011). Inflation and deflation at the steep-sided Llaima stratovolcano (Chile) detected by using InSAR. *Geophys. Res. Lett.*, 38(10):1–5.
- Bathke, H., Sudhaus, H., Holohan, E., Walter, T. R., and Shirzaei, M. (2013). An active ring fault detected at Tendürek volcano by using InSAR. *J. Geophys. Res. Solid Earth*, 118(8):4488–4502.
- Bekaert, D. P., Walters, R. J., Wright, T. J., Hooper, A. J., and Parker, D. J. (2015). Statistical comparison of InSAR tropospheric correction techniques. *Remote Sens. Environ.*, 170:40–47.
- Biggs, J., Ebmeier, S. K., Aspinall, W. P., Lu, Z., Pritchard, M. E., Sparks, R. S., and Mather, T. A. (2014). Global link between deformation and volcanic eruption quantified by satellite imagery. *Nat. Commun.*, 5(3471).
- Chadwick, W. W., Jónsson, S., Geist, D. J., Poland, M. P., Johnson, D. J., Spencer, B., Harpp, K. S., and Ruiz, A. (2011). The May 2005 eruption of Fernandina volcano, Galápagos: The first circumferential dike intrusion observed by GPS and InSAR. *Bull. Volcanol.*, 73(6):679–697.

552 Ching, J. and Chen, Y.-C. (2007). Transitional Markov Chain Monte Carlo method for Bayesian  
 553 model updating, model class selection, and model averaging. *J. Eng. Mech.*, 133(7):816–832.

554 Cirella, A., Piatanesi, A., Cocco, M., Tinti, E., Scognamiglio, L., Michelini, A., Lomax, A., and  
 555 Boschi, E. (2009). Rupture history of the 2009 L’Aquila (Italy) earthquake from non-linear joint  
 556 inversion of strong motion and GPS data. *Geophys. Res. Lett.*, 36(19):1–6.

557 Dalcin, L. D., Paz, R. R., Kler, P. A., and Cosimo, A. (2011). Parallel distributed computing using  
 558 Python. *Adv. Water Resour.*, 34(9):1124–1139.

559 Das, S. (2015). *Supershear Earthquake Ruptures – Theory, Methods, Laboratory Experiments and*  
 560 *Fault Superhighways: An Update*, chapter 1, pages 1–20. Springer International Publishing,  
 561 Cham.

562 Dettmer, J., Benavente, R., Cummins, P. R., and Sambridge, M. (2014). Trans-dimensional finite-  
 563 fault inversion. *Geophys. J. Int.*, 199(2):735–751.

564 Dettmer, J. and Dosso, S. E. (2012). Trans-dimensional matched-field geoacoustic inversion with  
 565 hierarchical error models and interacting Markov chains. *J. Acoust. Soc. Am.*, 132(4):2239–2250.

566 Dettmer, J., Dosso, S. E., and Holland, C. W. (2007). Uncertainty estimation in seismo-acoustic  
 567 reflection travel time inversion. *J. Acoust. Soc. Am.*, 122(1):161–176.

568 Duputel, Z., Agram, P. S., Simons, M., Minson, S. E., and Beck, J. L. (2014). Accounting for  
 569 prediction uncertainty when inferring subsurface fault slip. *Geophys. J. Int.*, 197(1):464–482.

570 Duputel, Z., Rivera, L., Fukahata, Y., and Kanamori, H. (2012). Uncertainty estimations for  
 571 seismic source inversions. *Geophys. J. Int.*, 190(2):1243–1256.

572 Dutta, R., Jónsson, S., and Vasyura-Bathke, H. (2019). Simultaneous Bayesian estimation of  
 573 non-planar fault geometry and spatially-variable slip. *J. Geophys. Res. Solid Earth (in review)*.

574 Dutta, R., Jónsson, S., Wang, T., and Vasyura-Bathke, H. (2018). Bayesian estimation of source  
 575 parameters and associated Coulomb failure stress changes for the 2005 Fukuoka ( Japan ) earth-  
 576 quake. *Geophys. J. Int.*, 213:261–277.

577 Fukuda, J. and Johnson, K. M. (2008). A fully Bayesian inversion for spatial distribution of fault  
 578 slip with objective smoothing. *Bull. Seismol. Soc. Am.*, 98(3):1128–1146.

579 Geyer, C. J. (1991). Markov Chain Monte Carlo Maximum Likelihood. In *Computing Science and*  
580 *Statistics, Proceedings of the 23rd Symposium on the Interface*, pages 156–163.

581 Hallo, M. and Gallovic, F. (2016). Fast and cheap approximation of Green function uncertainty  
582 for waveform-based earthquake source inversions. *Geophys. J. Int.*, 207:1012–1029.

583 Hartzell, S. H. and Heaton, T. H. (1983). Inversion of strong ground motion and teleseismic  
584 waveform data for the fault rupture history of the 1979 Imperial Valley, California, earthquake.  
585 *Bull. Seismol. Soc. Am.*, 73(6):1553–1583.

586 Haskell, N. A. (1964). Total energy and energy spectral density of elastic wave radiation from  
587 propagating faults. *Bull. Seismol. Soc. Am.*, 54(6):1811–1841.

588 Hastings, W. K. (1970). Monte Carlo sampling methods using Markov chains and their applications.  
589 *Biometrika*, 57(1):97–109.

590 Heimann, S. (2011). *A robust method to estimate kinematic earthquake source parameters*. PhD  
591 thesis, University of Hamburg.

592 Heimann, S., Kriegerowski, M., Isken, M., Cesca, S., Daout, S., Grigoli, F., Juretzek, C., Megies,  
593 T., Nooshiri, N., Steinberg, A., Sudhaus, H., Vasyura-Bathke, H., Willey, T., and Dahm, T.  
594 (2017). Pyrocko - An open-source seismology toolbox and library. *GFZ Data Services*, v. 0.3.  
595 doi:10.5880/GFZ.2.1.2017.001.

596 Heimann, S., Vasyura-Bathke, H., Sudhaus, H., Isken, M. P., Kriegerowski, M., Steinberg, A., and  
597 Dahm, T. (2019). A Python framework for efficient use of pre-computed Green’s functions in  
598 seismological and other physical forward and inverse source problems. *Solid Earth*, 10(6):1921–  
599 1935.

600 Hunter, J. D. (2007). Matplotlib : A 2D graphics environment. *Computing in Science & Engi-*  
601 *neering*, 9(3):90–95.

602 Isken, M., Sudhaus, H., Heimann, S., Steinberg, A., Daout, S., and Vasyura-Bathke, H. (2017).  
603 Kite - Software for Rapid Earthquake Source Optimisation from InSAR Surface Displacement.  
604 *GFZ Data Services*, v 0.1. doi:10.5880/GFZ.2.1.2017.002.

605 Jarzynski, C. (1997). Equilibrium free energy differences from nonequilibrium measurements: a  
606 master equation approach. *Phys. Rev. Lett.*, 78(14):2690–2693.

607 Jasra, A., Stephens, D. A., and Holmes, C. C. (2007). On population-based simulation for static  
608 inference. *Statist. Comput.*, 17(3):263–279.

609 Ji, C., Wald, D. J., and Helmberger, D. V. (2002). Source description of the 1999 Hector Mine,  
610 California, earthquake, part I: Wavelet domain inversion theory and resolution analysis. *Bull.*  
611 *Seismol. Soc. Am.*, 92(4):1192–1207.

612 Jolivet, R., Lasserre, C., Doin, M.-P., Guillaso, S., Peltzer, G., Dailu, R., Sun, J., Shen, Z.-K.,  
613 and Xu, X. (2012). Shallow creep on the Haiyuan Fault (Gansu, China) revealed by SAR  
614 Interferometry. *J. Geophys. Res.*, 117(B6):B06401.

615 Jónsson, S., Zebker, H., Segall, P., and Amelung, F. (2002). Fault slip distribution of the 1999 Mw  
616 7.1 Hector Mine, California, earthquake, estimated from satellite radar and GPS measurments.  
617 *Bull. Seismol. Soc. Am.*, 92(4):1377–1389.

618 Jost, M. L. and Herrmann, R. B. (1989). A student’s guide to and review of moment tensors.  
619 *Seismol. Res. Lett.*, 60(2):37–57.

620 Kennett, B. L. N., Engdahl, E. R., and Buland, R. (1995). Constraints on seismic velocities in the  
621 Earth from traveltimes. *Geophys. J. Int.*, 122:108–124.

622 Kikuchi, M. and Kanamori, H. (1982). Inversion of complex body waves. *Bull. Seismol. Soc. Am.*,  
623 72(2):491–506.

624 Kumagai, H., Maeda, Y., Ichihara, M., Kame, N., and Kusakabe, T. (2014). Seismic moment and  
625 volume change of a spherical source. *Earth, Planets and Space*, 66(7):1–10.

626 Mai, M. P., Shearer, P., Ampuero, J.-P., and Lay, T. (2016a). Standards for documenting finite-  
627 fault earthquake rupture models. *Seismol. Res. Lett.*, 87(3):712–718.

628 Mai, P. M., Schorlemmer, D., Page, M., Asano, K., Causse, M., Custodio, S., Festa, G., Galis, M.,  
629 Gallovic, F., Imperatori, W., Käser, M., Malytsky, D., Okuwaki, R., Pollitz, F., Razafindrakoto,  
630 H. N. T., Sekiguchi, H., Song, S. G., Somala, S. N., Thingbaijam, K. K. S., Twardzik, C., Driel,

631 V., Vyas, J. C., Wang, R., Yagi, Y., and Zielke, O. (2016b). The earthquake-source inversion  
632 validation ( SIV ) project. *Seismol. Res. Lett.*, 87(3):690–708.

633 Mai, P. M. and Thingbaijam, K. K. S. (2014). SRCMOD: An online database of finite-fault rupture  
634 models. *Seismol. Res. Lett.*, 85(6):1348–1357.

635 Met Office (2015). *Cartopy: a cartographic python library with a Matplotlib interface*. Exeter,  
636 Devon.

637 Metropolis, N., Rosenbluth, A. W., Rosenbluth, M. N., Teller, A. H., and Teller, E. (1953). Equa-  
638 tion of state calculations by fast computing machines. *J. Chem. Phys.*, 1087(21):1087–1092.

639 Minson, S. E., Simons, M., and Beck, J. L. (2013). Bayesian inversion for finite fault earthquake  
640 source models I-theory and algorithm. *Geophys. J. Int.*, 194(3):1701–1726.

641 Monelli, D. and Mai, P. M. (2008). Bayesian inference of kinematic earthquake rupture parameters  
642 through fitting of strong motion data. *Geophys. J. Int.*, 173(1):220–232.

643 Moral, P. D., Doucet, A., and Jasra, A. (2006). Sequential Monte Carlo samplers. *J.R. Statist.*  
644 *Soc. B.*, 68(3):411–436.

645 Mosegaard, K. (2012). Limits to Nonlinear Inversion. In Jónasson, K., editor, *Applied Parallel and*  
646 *Scientific Computing*, pages 11–21, Berlin, Heidelberg. Springer Berlin Heidelberg.

647 Neal, R. M. (2001). Annealed importance sampling. *Statist. Comput.*, 11(2):125–139.

648 Okada, Y. (1985). Surface deformation due to shear and tensile faults in a half-space. *Bull. Seismol.*  
649 *Soc. Am.*, 75(4):1135–1154.

650 Olsen, A. H. and Apsel, R. J. (1982). Finite faults and inverse theory with applications to the  
651 1979 Imperial Valley Earthquake. *Bull. Seismol. Soc. Am.*, 72(6):1969–2001.

652 Pugh, D. J. and White, R. S. (2018). MTfit: A Bayesian approach to seismic moment tensor  
653 inversion. *Seismol. Res. Lett.*, 89(4):1507–1513.

654 Ragon, T., Sladen, A., and Simons, M. (2018). Accounting for uncertain fault geometry in earth-  
655 quake source inversions - I: Theory and simplified application. *Geophys. J. Int.*, 214(2):1174–  
656 1190.

657 Razafindrakoto, H. N. T. and Mai, M. P. (2014). Uncertainty in earthquake source imaging due to  
658 variations in source time function and earth structure. *Bull. Seismol. Soc. Am.*, 104(2):855–874.

659 Roberts, G. O. and Rosenthal, J. S. (2001). Optimal scaling for various Metropolis-Hastings  
660 algorithms. *Statistical Science*, 16(4):351–367.

661 Salvatier, J., Wiecki, T., and Fonnesbeck, C. (2015). Probabilistic programming in Python using  
662 PyMC. *PeerJ Comput. Sci.*, 2:e55.

663 Sambridge, M. and Mosegaard, K. (2002). Monte Carlo Methods in Geophysical Inverse Problems.  
664 *Rev. Geophys.*, 40(September).

665 Sokos, E., Zahradník, J., Kiratzi, A., Janský, J., Gallovič, F., Novotný, O., Kostecký, J., Serpet-  
666 sidaki, A., and Tselentis, G. A. (2012). The January 2010 Efpalio earthquake sequence in the  
667 western Corinth Gulf (Greece). *Tectonophysics*, 530-531:299–309.

668 Stähler, S. C. and Sigloch, K. (2014). Fully probabilistic seismic source inversion – Part 1 : Efficient  
669 parameterisation. *Solid Earth*, 5:1055–1069.

670 Sudhaus, H. and Jónsson, S. (2009). Improved source modelling through combined use of InSAR  
671 and GPS under consideration of correlated data errors: application to the June 2000 Kleifarvatn  
672 earthquake, Iceland. *Geophys, J. Int.*, 176(2):389–404.

673 Sudhaus, H. and Jónsson, S. (2011). Source model for the 1997 Zirkuh earthquake (MW = 7.2) in  
674 Iran derived from JERS and ERS InSAR observations. *Geophys, J. Int.*, 185:676–692.

675 Tape, W. and Tape, C. (2012). A geometric setting for moment tensors. *Geophys, J. Int.*,  
676 190(1):476–498.

677 Tape, W. and Tape, C. (2015). A uniform parametrization of moment tensors. *Geophys, J. Int.*,  
678 202(3):2074–2081.

679 Tarantola, A. and Valette, B. (1982). Inverse Problems = Quest for Information. *J. Geophys.*,  
680 50:159–170.

681 Theano Development Team (2016). Theano: A Python framework for fast computation of mathe-  
682 matical expressions. *arXiv e-prints*, abs/1605.0.

683 Vackář, J., Burjánek, J., Gallovič, F., Zahradník, J., and Clinton, J. (2017). Bayesian ISOLA: New  
684 tool for automated centroid moment tensor inversion. *Geophys. J. Int.*, 210(2):693–705.

685 Vasyura-Bathke, H., Dettmer, J., Steinberg, A., Heimann, S., Isken, M., Zielke, O., Mai, P. M.,  
686 Sudhaus, H., and Jónsson, S. (2019). BEAT - Bayesian Earthquake Analysis Tool. *GFZ Data*  
687 *Services*, v.1.0. doi:10.5880/fdgeo.2019.024.

688 Wang, R. (1999). A simple orthonormalization method for stable and efficient computation of  
689 Green’s functions. *Bull. Seismol. Soc. Am.*, 89(3):733–741.

690 Wang, R., Heimann, S., Zhang, Y., Wang, H., and Dahm, T. (2017). Complete synthetic seismo-  
691 grams based on a spherical self-gravitating Earth model with an atmosphere – ocean – mantle  
692 – core structure. *Geophys. J. Int.*, 210:1739–1764.

693 Wang, R., Lorenzo-Martín, F., and Roth, F. (2006). PSGRN / PSCMP — a new code for calcu-  
694 lating co- and post-seismic deformation , geoid and gravity changes based on the viscoelastic-  
695 gravitational dislocation theory. *Comput. Geosci.*, 32(4):527–541.

696 Xu, W., Dutta, R., and Jonsson, S. (2015). Identifying active faults by improving earthquake  
697 locations with InSAR data and Bayesian estimation: The 2004 Tabuk (Saudi Arabia) earthquake  
698 sequence. *Bull. Seismol. Soc. Am.*, 105(2A):765–775.

699 Yagi, Y. and Fukahata, Y. (2011). Introduction of uncertainty of Green’s function into waveform  
700 inversion for seismic source processes. *Geophys. J. Int.*, 186(2):711–720.

701 Zhang, Y., Feng, W., Chen, Y., Xu, L., Li, Z., and Forrest, D. (2012). The 2009 L’Aquila M W  
702 6.3 earthquake: A new technique to locate the hypocentre in the joint inversion of earthquake  
703 rupture process. *Geophys. J. Int.*, 191(3):1417–1426.

704 **List of mailing addresses of all authors**

705 Hannes Vasyura-Bathke

706 hvasbath@uni-potsdam.de

707

708 Jan Dettmer

709 jan.dettmer@ucalgary.ca

710

711 Andreas Steinberg

712 andreas.steinberg@ifg.uni-kiel.de

713

714 Sebastian Heimann

715 sebastian.heimann@gfz-potsdam.de

716

717 Marius Isken

718 marius.isken@gfz-potsdam.de

719

720 Olaf Zielke

721 olaf.zielke@kaust.edu.sa

722

723 Paul Martin Mai

724 martin.mai@kaust.edu.sa

725

726 Henriette Sudhaus

727 henriette.sudhaus@ifg.uni-kiel.de

728

729 Sigurjón Jónsson

730 sigurjon.jonsson@kaust.edu.sa

731

## 732 List of figure captions

733 *Figure 1:* The BEAT modular program structure. The main **problem** objects determine, to-  
734 gether with their **composites**, the model that contains the rules to calculate the posterior prob-  
735 ability. To date, BEAT contains two **problem** classes, the geometry problem (Sec. 2.2) and the  
736 finite-fault estimation problem (Sec.: 2.3). These are being used by the **sampler** objects to explore  
737 the solution space of their respective PPD.

738

739 *Figure 2:* An example of a directory tree for a BEAT project after all steps have been executed.  
740 The **config\_\*.yaml** files are the parameter files to configure and customize the sampling pro-  
741 cess. The **results** directory (created by command **export**) contains sampling results, estimated  
742 covariance matrices and synthetics. The **hypers** directory contains sampling results of the initial  
743 hyper-parameter estimation. The **linear\_gfs** directory contains the Green's functions for the  
744 finite-fault-inversion (created by command **build\_gfs**). **stage\_\*** folders contain results of the dif-  
745 ferent sampling stages of the SMC sampler ("\*" represents the integer number of the corresponding  
746 stage) and **stage\_-1** contains the PPD of the model parameters of the corresponding final stage.

747

748 *Figure 3:* Results of Example 1: (a) and (b) Hudson plots from ensembles of 1000 moment-tensor  
749 solutions (small black beachballs) for estimations using variance and non-Toeplitz covariance data-  
750 covariance matrices, respectively. The large red and grey beachballs show the MAP solutions and  
751 the true moment tensor, respectively. (c) and (d) fuzzy beachballs based on ensembles of 1000  
752 MT solutions drawn from the PPD of the two estimations using the variance and non-Toeplitz  
753 data-covariance matrices, respectively.

754

755 *Figure 4:* Results of Example 2: Marginal posterior distributions for model parameters of a double-  
756 couple source estimated from real teleseismic data of the L'Aquila earthquake obtained from two  
757 different sampling algorithms, Sequential Monte Carlo (SMC, yellow) and Parallel Tempering (PT,  
758 blue). The MAP values are marked by vertical colored lines.

759

760 *Figure 5:* Results of Example 3: 1D and 2D marginal posteriors of a rectangular source for the

761 L'Aquila earthquake. The red vertical lines in the histograms and the red dot in the 2d correlation  
762 maps mark the MAP solution. In the correlation plots, blue colors are regions of high probability.  
763 North and East shifts are relative to a given reference location.

764

765 *Figure 6:* Results of Example 4: a) Static slip distribution solution for the L'Aquila 2009 earth-  
766 quake estimated using static InSAR surface displacements. The patch colors and the black arrows  
767 show the MAP, whereas the black ellipses around the arrow tips show the two-sigma confidence  
768 bounds.

769

770 *Figure 7:* Results of Example 5: (a) Kinematic slip distribution for the L'Aquila 2009 earthquake  
771 from the joint inference on teleseismic and InSAR static data. The patch colors and the black  
772 arrows show the MAP, whereas the black ellipses around the arrow tips indicate the two-sigma  
773 confidence boundaries, and the black star marks the hypocentral location. The black continuous  
774 lines show the MAP of the evolving rupture front, with the timing of each front in seconds anno-  
775 tated on the respective isoline. The uncertainty of the rupture onset time is shown as the fuzzy  
776 isolines with light grey indicating lower probability. (b) The ensemble of moment rate function  
777 solutions, with dark and red colors indicating high probability moment rates. The continuous black  
778 line shows the MAP moment rate function. (c) Marginal posterior distribution for the Laplacian  
779 smoothing weight  $\alpha$ , with the red vertical line marking the MAP solution.

780

781 *Figure 8:* Results of Example 5: geodetic InSAR data fits for the L'Aquila earthquake from  
782 descending (a) and ascending (b) acquisition geometry. (data panels) Geocoded unwrapped in-  
783 terferograms in radar line-of-sight (LOS) with negative values indicating increasing LOS distance  
784 due to subsidence. The displayed displacement values are derived from quadtree subsampling and  
785 extrapolated to each pixel that belong to the same quadtree square. The look-vector and heading  
786 of the satellite are shown by the two short and long arrows, respectively. (model panels) Synthetic  
787 surface displacements in LOS derived from the MAP solution. The small grey rectangle shows  
788 the location and orientation of the derived fault geometry from example 2, whereas the red rect-  
789 angle shows the extended fault geometry that is used in examples 3 and 4. The solid black lines

mark the upper edge of the fault. (residual panels) Residual surface displacements, i.e., the difference between the model and the data panels. Note the different color scale for the residual plots.

*Figure 9:* Results of Example 5: Waveform fits for the kinematic finite fault solution for P-wave arrivals for 16 of the 35 stations used. The filtered (0.001-0.5Hz) displacement waveform data (dark grey solid line) and the filtered synthetic displacement waveforms (red solid line) are shown together, with the brown shading indicating 100 random draws of the filtered synthetic displacements from the PPD. The residual waveforms are shown below each waveform as filled red-line polygons. Each trace box is annotated with the station name and component, as well as the distance and azimuth from the MAP solution of the center of the reference fault. The arrival time and the duration of each window are shown in the lower left and right, respectively.



Table 1: Recent, open source software for Bayesian estimation of deformation sources.

NAME	UQ, SAMPLERS <sup>a</sup>	SOURCE TYPES	SOURCE FUNCTION(STF)	DATA TYPES	GF SUP-PORT <sup>b</sup>	REFERENCES
MTfit	Bayesian, MH <sup>c</sup> , RJMCMC <sup>d</sup> , MC <sup>e</sup>	single source, linear full MT <sup>f</sup> , DC <sup>g</sup>	no	wave polarity, wave amplitude ratios	no	[Pugh and White, 2018]
GBIS	Bayesian, AMH <sup>h</sup>	multiple sources, isotropic point, spherical, rectangular, penny-shaped crack, ellipsoid	no	static displacements (GNSS <sup>i</sup> , InSAR <sup>j</sup> )	half-space only	[Bagnardi and Hooper, 2018]
Bayes ISOLA	Bayesian, grid search, LSQ <sup>k</sup>	single source, quasi-nonlinear full MT	no	seismogram waveforms	yes	[Vackář et al., 2017]
BEAT	Bayesian, AMH, SMC <sup>l</sup> , PT <sup>m</sup>	multiple sources, nonlinear full MT, rectangular source, isotropic MT, CLVD <sup>n</sup> , DC; full kinematic/static finite-fault	half-sinusoidal, triangular, boxcar	seismogram waveforms, static displacements (GNSS, InSAR)	yes	this work

<sup>a</sup>UQ- uncertainty quantification

<sup>b</sup>GF- Green's Function

<sup>c</sup>MH- Metropolis-Hastings

<sup>d</sup>RJCMCMC- reversible jump markov chain monte carlo

<sup>e</sup>MC- Monte Carlo random sampling

<sup>f</sup>MT- moment tensor

<sup>g</sup>DC- double couple

<sup>h</sup>AMH- Adaptive Metropolis-Hastings

<sup>i</sup>GNSS- global navigation satellite system

<sup>j</sup>InSAR- interferometric synthetic aperture radar

<sup>k</sup>LSQ- least squares inversion

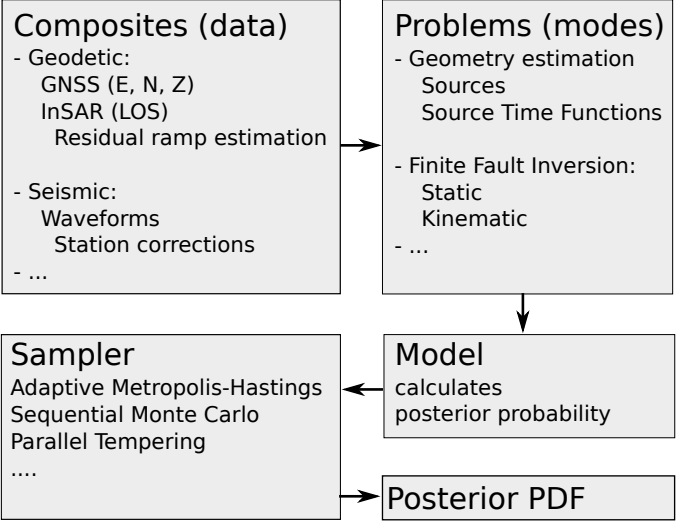
<sup>l</sup>SMC- sequential Monte Carlo

<sup>m</sup>PT- parallel tempering

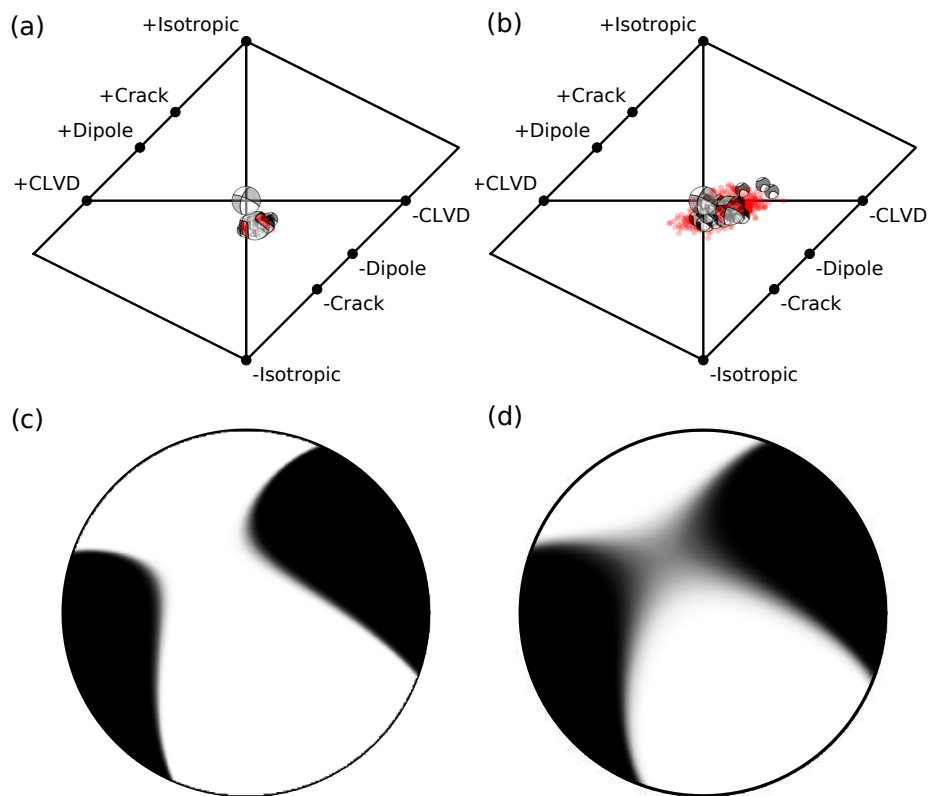
<sup>n</sup>CLVD- compensated linear vector dipole

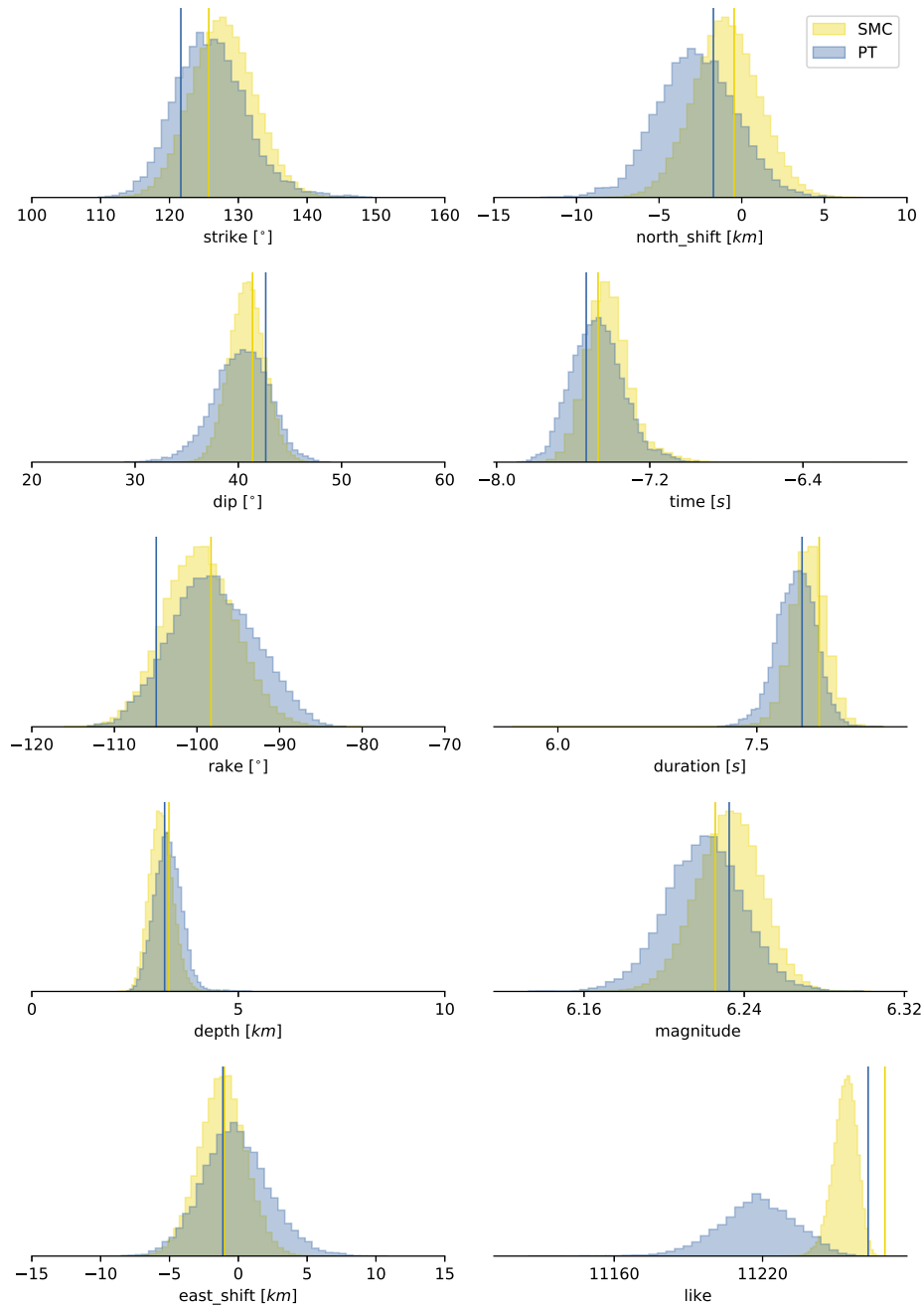
Table 2: Types of deformation sources and their source specific parameters that can be estimated in the **geometry** mode of BEAT.

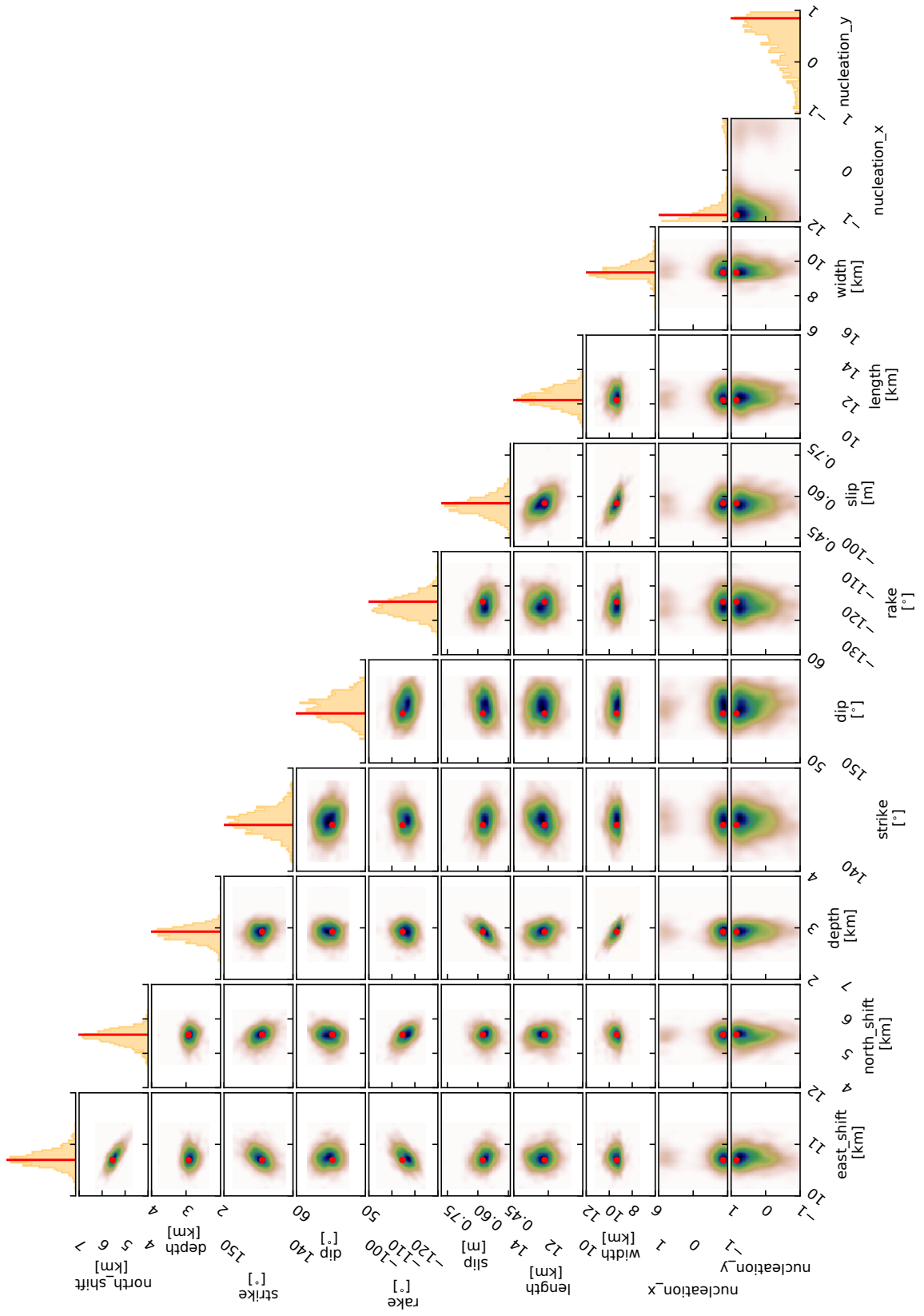
DEFORMATION SOURCE	PARAMETERS <b>m</b>	REFERENCES
Full moment tensor (MT) I	$m_{nn}, m_{ee}, m_{dd}, m_{ne}, m_{nd}, m_{ed}$ , moment magnitude	[ <a href="#">Stähler and Sigloch, 2014</a> ]
Full moment tensor (MT) II	$u, v, \kappa, \sigma, h$ , moment magnitude	[ <a href="#">Tape and Tape, 2015</a> ]
Isotropic moment tensor	moment magnitude or volume change	[ <a href="#">Kumagai et al., 2014</a> ]
Double couple (DC)	strike, dip, rake, moment magnitude	[ <a href="#">Jost and Herrmann, 1989</a> ]
Compensated linear vector dipole (CLVD)	dip, azimuth (of largest dipole), moment magnitude	[ <a href="#">Jost and Herrmann, 1989</a> ]
Rectangular source	strike, dip, rake, length, width, slip, optional: hypocentral location (x,y), rupture velocity	[ <a href="#">Haskell, 1964</a> ]

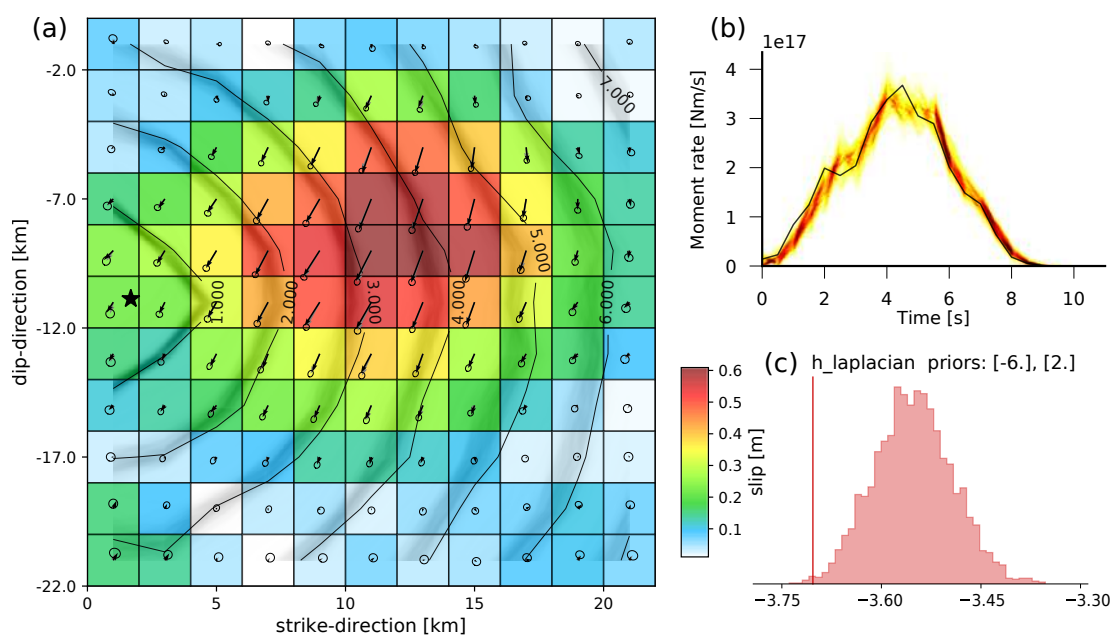
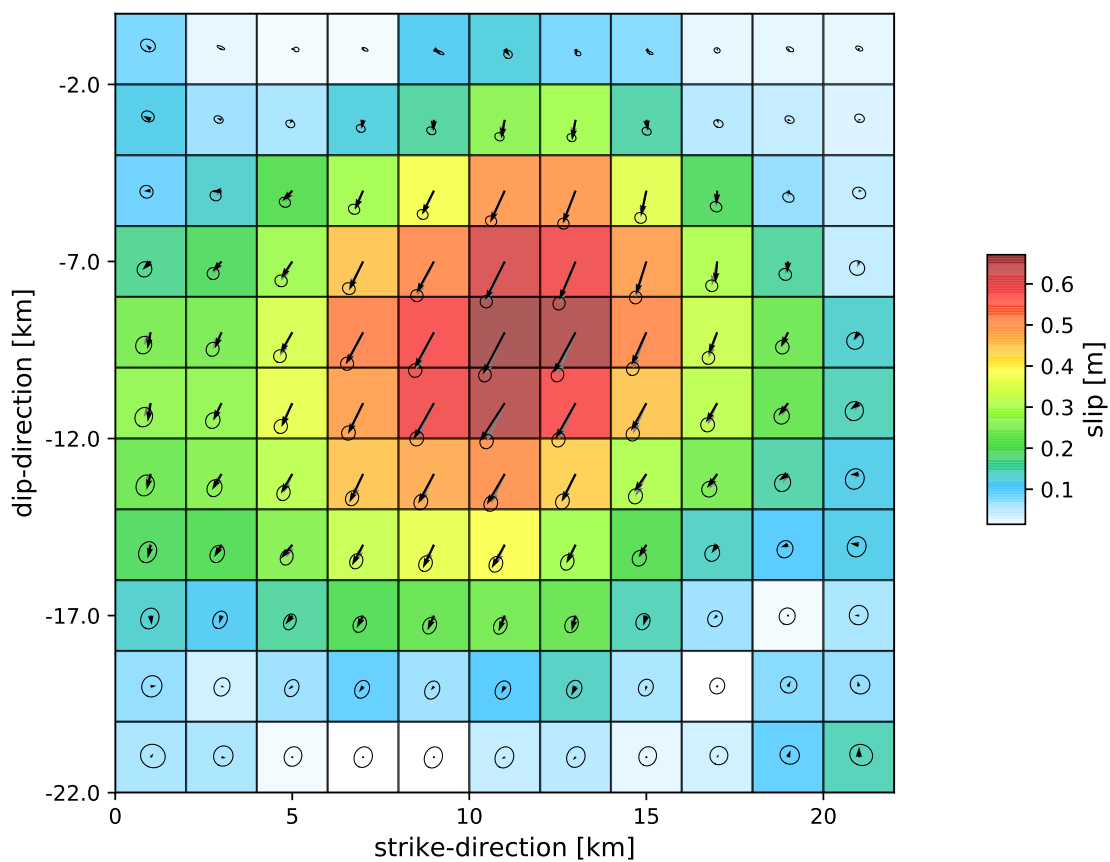


```
Laquila2009
├── BEAT_log.txt
├── config_ffi.yaml
├── config_geometry.yaml
├── ffi
│   ├── figures
│   ├── hypers
│   ├── linear_gfs
│   ├── results
│   └── stage_*
├── geodetic_data.pkl
├── geometry
│   ├── figures
│   ├── hypers
│   ├── results
│   └── stage_*
└── seismic_data.pkl
```

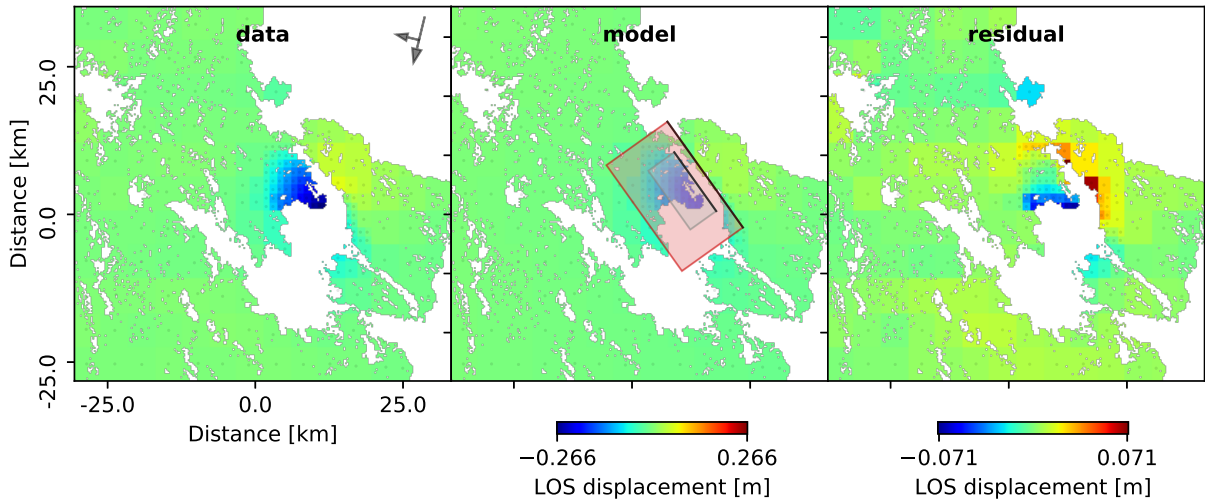




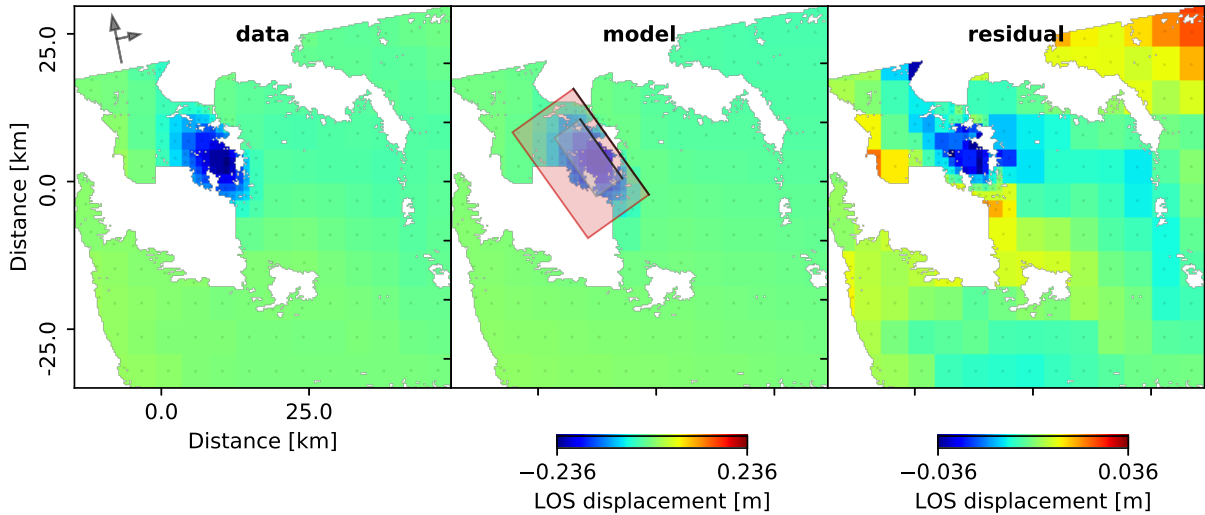




data



(b) ascending



Z (1/2, 1/2)

